Biofabrication

International Society for Biofabrication

PAPER • **OPEN ACCESS**

In vivo organized neovascularization induced by 3D bioprinted endothelial-derived extracellular vesicles

To cite this article: Fabio Maiullari *et al* 2021 *Biofabrication* **13** 035014

View the article online for updates and enhancements.

You may also like

- The rise of electric vehicles—2020 status and future expectations
Matteo Muratori, Marcus Alexander, Doug Arent et al.
- The size and range effect: lifecycle greenhouse gas emissions of electric vehicles
Linda Ager-Wick Ellingsen, Bhawna Singh and Anders Hammer Strømman
- Electric Vehicles Charging Scheduling Strategy Considering the Uncertainty of Photovoltaic Output
Xiangxiang Wei, Su Su, Yunli Yue et al.

BREATH® BIOPSY

Breath Biopsy® OMNI

The most advanced, complete solution for global breath biomarker analysis

SEE WHAT OMNI CAN DO FOR YOU

Expert Study Design & Management

Robust Breath Collection

Reliable Sample Processing & Analysis

In-depth Data Analysis

Specialist Data Interpretation

This content was downloaded from IP address 80.169.235.78 on 16/11/2021 at 09:42

Biofabrication

PAPER

In vivo organized neovascularization induced by 3D bioprinted endothelial-derived extracellular vesicles

Fabio Maiullari[1,2], Maila Chirivì[2,3], Marco Costantini[4], Anna Maria Ferretti[5], Sandro Recchia[6], Silvia Maiullari[3,7], Marika Milan[2,3], Dario Presutti[3,4], Valentina Pace[3,8], Marcello Raspa[3], Ferdinando Scavizzi[3], Massimo Massetti[9], Lella Petrella[10], Mara Fanelli[10], Marta Rizzi[11], Orazio Fortunato[12], Fabiola Moretti[3,13], Eugenio Caradonna[14], Claudia Bearzi[2,3] and Roberto Rizzi[2,15]

[1] Gemelli Molise SpA, Campobasso, Italy
[2] Istituto Nazionale Genetica Molecolare INGM 'Romeo ed Enrica Invernizzi', Milan, Italy
[3] Institute of Biochemistry and Cell Biology, National Research Council of Italy (IBBC-CNR), Monterotondo, Rome, Italy
[4] Institute of Physical Chemistry, Polish Academy of Sciences, Warsaw, Poland
[5] Institute of Chemical Sciences and Technologies "Giulio Natta", National Research Council of Italy (SCITEC-CNR), Milano, Italy
[6] Department of Science and High Technology, University of Insubria, Como, Italy
[7] Institute of Pathology, Università Cattolica del Sacro Cuore, Rome, Italy
[8] Department of Experimental Medicine, Sapienza University of Rome, Rome, Italy
[9] Department of Cardiovascular Disease, IRCCS Fondazione Policlinico Universitario Agostino Gemelli, Rome, Italy
[10] Laboratory of Molecular Oncology, Gemelli Molise SpA, Campobasso, Italy
[11] Ufficio Programmazione e Grant Office, National Research Council of Italy (UPGO-CNR), Rome, Italy
[12] Tumor Genomics Unit, Department of Research, IRCCS Fondazione Istituto Nazionale dei Tumori, Milan, Italy
[13] IRCCS Regina Elena National Cancer Institute, Rome, Italy
[14] Research Unit, Gemelli Molise SpA, Campobasso, Italy
[15] Institute of Biomedical Technologies, National Research Council of Italy (ITB-CNR), Segrate, Milan, Italy

E-mail: roberto.rizzi@cnr.it

OPEN ACCESS

RECEIVED
9 December 2020

ACCEPTED FOR PUBLICATION
12 January 2021

PUBLISHED
7 April 2021

Original content from this work may be used under the terms of the Creative Commons Attribution 4.0 licence.

Any further distribution of this work must maintain attribution to the author(s) and the title of the work, journal citation and DOI.

Keywords: 3D bioprinting, extracellular vesicles, innovative bioinks, neovascularization

Supplementary material for this article is available online

Abstract

Extracellular vesicles (EVs) have become a key tool in the biotechnological landscape due to their well-documented ability to mediate intercellular communication. This feature has been explored and is under constant investigation by researchers, who have demonstrated the important role of EVs in several research fields ranging from oncology to immunology and diagnostics to regenerative medicine. Unfortunately, there are still some limitations to overcome before clinical application, including the inability to confine the EVs to strategically defined sites of interest to avoid side effects. In this study, for the first time, EV application is supported by 3D bioprinting technology to develop a new strategy for applying the angiogenic cargo of human umbilical vein endothelial cell-derived EVs in regenerative medicine. EVs, derived from human endothelial cells and grown under different stressed conditions, were collected and used as bioadditives for the formulation of advanced bioinks. After *in vivo* subcutaneous implantation, we demonstrated that the bioprinted 3D structures, loaded with EVs, supported the formation of a new functional vasculature *in situ*, consisting of blood-perfused microvessels recapitulating the printed pattern. The results obtained in this study favour the development of new therapeutic approaches for critical clinical conditions, such as the need for prompt revascularization of ischaemic tissues, which represent the fundamental substrate for advanced regenerative medicine applications.

1. Introduction

Biofabrication is an emerging research field covering a broad spectrum of biotechnological applications ranging from the *in vitro* modelling of 3D tissues to the recapitulation of complex physiological systems. The translational potential of this research field is evolving quickly, owing to the great support of the cell biology, materials science and bioengineering communities [1–3].

However, despite the ever-increasing resolution in cell deposition and the possibility of producing

© 2021 The Author(s). Published by IOP Publishing Ltd

heterogeneous constructs composed of multiple cell types and biomaterials, many challenges remain unmet. One of the most critical points concerns the integration of a functional vascular system within the biofabricated samples to prompt a blood supply and increase the chances of transplanted construct engraftment. This problem represents a bottleneck for many applications related to regenerative medicine, where the implanted tissue grafts need rapid integration with the host bloodstream to exchange nutrients and oxygen. Although the results obtained so far are encouraging, they are still linked to production methods and post-production processes that are too laborious and sometimes lack reproducibility [4, 5]. Therefore, new approaches should be developed that, on the one hand, should guarantee the rapid integration of tissue grafts with host microvasculature and, on the other hand, should offer the possibility of being easily integrated with other existing methods.

An alternative solution to solve this challenge could be offered by the use of immunoprivileged bioadditives for bioink formulation such as extracellular vesicles (EVs).

EVs are heterogeneous sub-micrometre particles fundamental to intercellular communication [6] which are rapidly emerging as therapeutic alternatives, to promote human tissue regeneration, and as predictive biomarkers [7–10]. In particular, EVs are functional cellular components [11] capable of transferring proteins [12], cytokines [13], mRNA [14], and noncoding RNA, such as microRNA [15] or long noncoding RNA [16], to surrounding cells, influencing their fate and behaviour [17]. These intercellular messengers are highly heterogeneous in cargo, membrane composition, biogenesis and size, which significantly correlate closely with defined biological functions [18]. The main subfamily is represented by microvesicles typically with dimensions between 200 nm and 1 μm in diameter, which are generated directly from the cell membrane [19]. The second subpopulation of EVs includes vesicles ranging from 30 to 120 nm in diameter, called exosomes. Exosomes can be considered the most studied family, and given their size, they are mainly responsible for the carriage of signalling molecules; they were first observed as intraluminal vesicles within endosomal multivesicular bodies (MVBs) released by cells after fusion of MVBs with the plasma membrane [20]. In particular, all exosomes show specific labelling depending on the type of cell of origin, sharing a precise subset of proteins involved in cell adhesion, structural dynamics, membrane fusion, metabolism, and signal transduction [21]. The interaction of EVs with target cells goes through three different molecular mechanisms: the fusion of lipid membranes [22], the activation of cell surface receptors by ligands or proteins [23–25], and the involvement of specific cellular processes, such as endocytosis, pinocytosis, or phagocytosis [26].

To date, many molecular dynamics, induced by EVs, have been well characterized, identifying specific protein, lipid, metabolic, and transcriptomic profiles, revealing their role in many biological processes, such as the recycling of membrane proteins and lipids, immune modulation, senescence, cell proliferation and differentiation, and last but not least, healthy or cancer-associated neoangiogenesis [14, 27–31].

A special mention should be made of EVs generated by endothelial cells (ECs) or endothelial precursor cells (EPCs) in the formation of new vessels [28, 29, 32]. Angiogenesis is a dynamic and tightly regulated process in which ECs, through crosstalk with the surrounding environment, secrete paracrine factors and develop cell–cell and cell–matrix functional interactions. Among the extracellular factors, EVs released by ECs, transporting on the surface vascular endothelial growth factor (VEGF), interleukin 6 (IL-6), IL-8, fibroblast growth factors (FGF) and plasminogen activator of urokinase type [12, 33], have been described as key players in the formation of blood vessels. For example, Taraboletti *et al* demonstrated that EVs released by ECs contain the enzymatically active matrix metalloproteinases 2 and 9, promoting EC invasion and capillary-like structure formation *in vitro* [34]. Interestingly, Sheldon *et al* showed that the δ-like 4-containing exosome stimulates the formation of capillary-like structures *in vitro* and *in vivo* through the internalization of the Notch receptor, followed by its degradation [35]. Meanwhile, Arderiu *et al* attributed the proangiogenic effect of the microparticles to the induction of β1 integrin expression in the target ECs, leading to Rac1-ERK1/2-ETS signalling and CCL2 production [36, 37]. Moreover, a growing number of studies have highlighted the role of hypoxia as a release stimulus and modulator of EV functions. These functions involve increased invasiveness and migration, proliferation, angiogenesis, and immunomodulation [38] owing to an increase in the enzymatic activity and the release of cytokines and proteins in hypoxic EVs compared to EVs isolated in normoxia conditions [39–42].

Nevertheless, EV therapeutic application, to date, has been strongly limited by the inability to confine EVs to a specific site of interest.

In this study, we demonstrate for the first time that EC-derived EVs can be employed as bioink additives and more effectively delivered *in vivo* when combined with a 3D bioprinting strategy, supporting the rapid neovascularization of bioprinted, cell-free grafts. In addition, we show *in vitro* that the new angiogenic message driven by the EVs is further extended to circulating EPC populations. Altogether, the presented results represent a simple yet robust platform to support the neovascularization of engineered tissues that enables one to bypass some of

the current limitations associated with the use of EVs *in vivo*, such as their uncontrolled spatial distribution [43–45].

2. Materials and methods

2.1. Human umbilical vein endothelial cell (HUVEC) culture

HUVECs were purchased from Thermo Fisher and cultured in Medium 200 (M200500, Gibco) supplemented with 2% v/v EV-depleted fetal bovine serum, hydrocortisone (1 μg ml^{-1}), human epidermal growth factor (10 ng ml^{-1}), basic FGF (3 ng ml^{-1}), and heparin (10 μg ml^{-1}) (S003K, Gibco), at 37 °C and 5% CO_2. HUVECs were expanded using trypsin-ethylenediaminetetraacetic acid (EDTA) up to the fifth passage.

2.2. Peripheral blood mononuclear cell (PBMC) isolation

PBMCs were isolated by Ficoll-Paque density gradient centrifugation. Buffy coats from healthy donors were diluted 1:1 with phosphate buffer saline (PBS) w/o Ca^{2+}/Mg^{2+}, layered onto Ficoll-Paque Plus (GE17-1440-02, Sigma) and centrifuged at 2000 rpm for 20 min at room temperature (RT). PBMCs were collected at the interface, washed twice with PBS and centrifuged at 1600 rpm for 10 min at RT. Finally, cells were incubated in red cell lysis buffer (1X) for 6 min, washed in PBS, resuspended in complete M200 medium, and used for the *in vitro* assay. Cell count and viability were evaluated by Trypan blue exclusion.

2.3. EV isolation

EVs were isolated from HUVEC-conditioned medium (HUVEC-derived EVs) collected from the following four experimental conditions: (a) complete M200 medium in normoxia (CM Normoxia); (b) complete M200 medium in hypoxia (CM Hypoxia); (c) serum-free M200 medium in normoxia (SM Normoxia); (d) serum-free M200 medium in hypoxia (SM Hypoxia). EV-depleted serum was used for the Complete M200 medium. After 48 h incubation in fresh medium, the conditioned media were collected and centrifuged at 500 g for 15 min and subsequently at 1000 g for 25 min at 4 °C to remove cell debris and organelles. Then, the supernatants were transferred into new tubes and ultracentrifuged using an L-90 Beckman centrifuge (Beckman Instruments, Inc., Fullerton, CA, USA) equipped with a Ti-70 rotor (Beckman Instruments) at 125 000 g for 90 min at 4 °C. Afterwards, the supernatants were discarded and the obtained EV pellets were resuspended and labelled using the Deep Red CellMask plasma membrane stain (1:5000; C10046, Molecular Probes) for 20 min at 37 °C. After further ultracentrifugation, the EVs were resuspended in 100 μl of PBS and used for the characterization [46] and 3D bioprinting experiments.

2.4. NanoSight analysis

Nanoparticles tracking analysis was performed using a NanoSight NS300 instrument (Malvern Panalytical). Five 30 s videos were recorded for each sample with a camera level set at 15/16 and a detection threshold set between 5 and 7. The EV concentration and size distribution were subsequently analysed with NTA 3.2 software.

2.5. Western blotting

Western blotting was performed using a sodium dodecyl sulphate–polyacrylamide gel electrophoresis (SDS–PAGE) system. EVs were lysed in RIPA buffer and proteins (40 μg) were loaded on 4%–12% Bis-Tris gel (Thermo Fisher Scientific) and transferred to PVDF membranes. Membranes were incubated with the following primary antibodies: anti-CD9 (1:1000, Cell Signaling), anti-CD81 (1:100, Thermo Fisher Scientific), and then the corresponding anti-mouse and anti-rabbit peroxidase-linked secondary antibodies (1:2000, GE Healthcare Life Sciences). Signal detection was performed via chemiluminescence reaction (ECL, GE Healthcare) using the MINI HD9 western blot imaging system (Cleaver Scientific Ltd, United Kingdom). Western blot quantification was achieved using ImageJ software analysis.

2.6. Flow cytometry

Flow cytometry analysis was accomplished as previously described by Théry *et al* [47]. Briefly, 30 μg of EVs were incubated with aldehyde/sulfate latex beads, 4% w/v (Thermo Fisher Scientific), for 15 min at RT and then in PBS overnight at 4 °C. EVs were fixed in 100 mM Glycine for 30 min at RT and afterwards stained with 1 μg of primary antibodies, anti-CD9 (Cell Signaling), anti-CD81 (Thermo Fisher Scientific), anti-CD63 (Abcam), for 30 min at 4 °C, followed by staining with fluorescent secondary antibodies Alexa Fluor 647-conjugated goat anti-rabbit IgG (Thermo Fisher Scientific) or Dylight 488-conjugated goat anti-mouse IgG (Bethyl). Samples were analysed using a flow cytometer (FACS Canto II, BD Biosciences) and FlowJo software (TreeStar).

2.7. Enzyme-linked immunosorbent assay (ELISA)

ELISA was performed to quantify the EV angiogenic ligand and receptor contents. EVs isolated from HUVECs, grown in different conditions, were lysed by incubation at 4 °C for 30 min in RIPA buffer, containing 50 mM Tris HCl pH 7.6, 150 mM NaCl, 0.5% sodium deoxycholate, 0.1% sodium dodecyl sulphate, 1% Triton, 1 mM EDTA (Sigma Aldrich), protease inhibitor cocktail (Sigma Aldrich), and phenylmethylsulfonyl fluoride (Sigma Aldrich). The concentration of proteins was quantified using Bradford reagents (Serva Electrophoresi) according to the

manufacturer's instructions. Bovine serum albumin (BSA) was used as a standard to determine the protein quantification.

Some 96-well microtiter ELISA plates were coated with 10 ng ml^{-1} VEGFA (583 706, BioLegend) or 5 ng ml^{-1} placental growth factor (PlGF, 590 706, BioLegend) and 500 ng ml^{-1} VEGF receptor 1 (VEGFR1, 321-FL, R&D Systems) or 500 ng ml^{-1} VEGF receptor 2 (VEGFR2, 595 006, BioLegend) recombinant proteins, and incubated overnight at RT. Subsequently, 5% BSA blocking solution was used to saturate the non-specific binding sites and PBS with 0.05% Tween-20 as washing buffer. A 10 ng/well dose of EV-derived proteins was added to detect ligands or receptors, respectively, and incubated for 1 h at 37 °C. Each plate was then incubated for 1 h at 37 °C with specific primary antibodies, anti-hVEGF (AF-293-Na, R&D Systems), anti-hPlGF (BAF264, R&D Systems), anti-hVEGFR1 (AF231, R&D Systems), anti-hVEGFR2 (AF257, R&D Systems), followed by biotinylated secondary antibody (BAF109, R&D Systems) diluted in 1% BSA. After extensive washing, the plates were first incubated for 1 h at RT with high-sensitivity Streptavidin–HRP conjugate (405 103, BioLegend) and then exposed for 20 min at RT to supersensitive 3,3′,5,5′-tetramethylbenzidine ELISA substrate (T-4444, Sigma Aldrich). The reaction was blocked using stop buffer solution. The absorbance was measured at 450 nm by an SAFAS Xenius XMA microplate reader. Standard curves were obtained using respective recombinant proteins.

2.8. Transmission electron microscopy (TEM) analysis

The isolated vesicles derived from the four experimental conditions were analysed using a Zeiss LIBRA 200FE-HR TEM, operating at 200 kV and equipped with a second-generation in-column W filter. The samples were prepared as described previously [48]. A drop of vesicle suspension was released on a Carbo/Formvar TEM grid, allowed to dry and then contrasted using UranyLess (EMS-Electron Microscopy Science).

Regarding the bioprinted samples, constructs containing EVs from starved and hypoxic HUVEC cultures were enzymatically digested with collagenase type 2 (LS004176, Worthington Biochemical Corporation) for 20 min at 37 °C, after 24 h of culture. Then, the EV suspension was centrifuged at 1000 *g* for 20 min at 4 °C to remove gelatin methacrylamide (GelMA) debris; the resulting supernatants were ultracentrifuged using an L-90 Beckman centrifuge (Beckman Instruments, Inc., Fullerton, CA, USA) equipped with a Ti-70 rotor (Beckman Instruments) at 125 000 *g* for 90 min at 4 °C. Finally, the obtained EVs were analysed by TEM using the procedure described above.

2.9. Bioink formulation, characterization, and 3D bioprinting

2.9.1. Bioink formulation

Gelatin (type A3 from porcine skin) methacrylamide (GelMA) was used to fabricate 3D bioprinted scaffolds and was prepared by reaction of gelatin with methacrylic anhydride. After the dissolution of gelatin in phosphate buffer (1 g/10 ml, pH 7.5) at 50 °C, 0.8 ml methacrylic anhydride was added dropwise under vigorous stirring. After 2 h, the reaction mixture was diluted and dialysed (MWCO = 2 kDa) for 3 d against distilled water at 40 °C and finally freeze-dried. The bioink stock solutions were prepared by dissolving 6% of GelMA w/v and 4% of low-molecular-weight alginate (ALG, FMC Biopolymers) w/v in 1 ml of 25 mM HEPES buffer (Sigma). After biopolymer dissolution, the bioink was filtered (0.22 μm) to guarantee sterile conditions. Each bioink was further loaded with EVs from one of the four different culturing conditions at a final concentration of 4×10^9 particles ml^{-1} of bioink stock solution. The experimental control group was formulated using the bioink stock solution without EVs (NO EVs). Finally, 1 mg ml^{-1} of Irgacure 2959 was added to the different bioinks to act as a radical photoinitiator.

2.9.2. Bioink rheological properties

The rheological properties of pure ALG (4% w/v), pure GelMA (6% w/v), ALG-GelMA and ALG-GelMA-EVs (EV concentration = 4×10^9 particles ml^{-1}) bioinks were analysed with a rotational rheometer (Anton Paar RHEOPLUS-32, plate–cone geometry). Solutions were kept under mild stirring at RT for ∼2 h before acquisition. The test was performed in a small closed chamber at 25 °C to prevent evaporation. Two loading cycles, with an interval of 10 min, were achieved before acquiring the rheological data.

2.9.3. Printability test

The formulated bioink was further tested to assess the range of calcium chloride and ALG concentrations in which a high printability can be obtained. Since the instantaneous crosslinking of our bioink is due to ALG, in this type of test we focused only on its concentration, in agreement with our previous study [49]. Accordingly, we have explored, for calcium chloride, the concentration range 0.3–0.6 M while for ALG 1%–4% w/v. The combined results have been plotted as a heat map (figure 3(B)) which helps to discern the best printing conditions for different ALG/-calcium chloride concentrations. Additionally, we have carried out another printability test using fixed concentrations of ALG and calcium chloride (the same used ultimately in this study, 4% w/v and 0.3 M) to investigate the dependence of the deposited fibre diameter on printing speed. Finally, our deposition strategy in combination with the formulated bioink

has been tested for the fabrication of scaffolds characterized by different fibre orientations (0°, 0°–90°, and 0°–30°–60°) and for the fabrication of a macroscopic, hierarchical vasculature model (see figure S4 (available online at stacks.iop.org/BF/13/035014/mmedia) in supplementary information).

2.9.4. 3D bioprinting

The bioinks and calcium chloride solution (0.3 M) were loaded in 1 ml sterile Hamilton glass syringes and connected to the internal and external needles of the dispensing coaxial nozzle system. NE-1000 Single Syringe Pumps (NewEra PumpSystems Inc.) were used to flow the bioinks and the crosslinking solution (printing speed = 200 mm min^{-1}, Q_{bioink} = 7 μl min^{-1}, Q_{CaCl2} = 5.4 μl min^{-1}). The printing speed and the flow rates were adjusted to obtain hydrogel fibres of approximately 200 μm in diameter. For all conditions, ten-layer-thick constructs were bioprinted with consecutively aligned organized fibres for each layer and 50 μm distance between hydrogel fibres in the *X*–*Y* plane. The result of the bioprinting process was a bioprinted cell-laden scaffold characterized by overall dimensions of 10 × 4 × 1 mm^3. After 3D bioprinting, samples were collected using a sterile spatula, placed in a 60 mm dish and UV-crosslinked at low light intensity (365 nm, 4–5 mW cm^{-2}) for 5 min. In parallel, bulks of hydrogel embedding EVs from starved and hypoxic HUVECs were prepared by casting the bioink in silicon moulds. Finally, the constructs were washed for 3 min with 5 mM EDTA solution (in 25 mM HEPES) to remove ALG from the hydrogel strands and used for *in vivo* and *in vitro* experiments.

2.10. Scanning electron microscopy (SEM) analysis

SEM images of the polymer with and without EVs were collected with an FEI ESEM-FEG XL30 microscope, operating at 10 kV in the low vacuum mode (sample chamber pressure = 1 torr), using a gas secondary electron detector. The following conditions were set up: working distance = 8 mm, spot size = 3, working temperature = 20 °C. All samples were prepared on different stubs and fixed to them by means of a double-sided adhesive carbon conductive tape. It was not necessary to cool all samples to improve their stability under the electron beam (up to 40 000× magnification).

2.11. Dispersion profile of bioprinted EVs

The bioprinted constructs containing EVs harvested from starved and hypoxic HUVECs were cultured in EV-free M200 medium to evaluate the anchoring of the EVs into the bioprinted structures. The conditioned medium was collected after 24 h, 48 h, 72 h, and 1 week of incubation at 37 °C, 5% CO_2 and stored at −20 °C. Samples were analysed by NanoSight NS300.

2.12. Subcutaneous implantation in mice

NSG and C57/BL6 mice (Jackson Laboratory) were used to evaluate the *in vivo* induced neovascularization through the bioprinted EVs derived from the different cell growth conditions. Two-month-old male mice (n = 3) were anaesthetized by 2% isoflurane inhalation. The backs of the animals were carefully shaved with an electric razor and sterilized with iodine solution. Afterward, the mice were placed on the operating table, warmed at 37 °C. Four limited skin incisions on the back medial sides were performed and the dorsal muscle was separated from the skin; the different constructs were carefully positioned in each pocket and the skin was sutured by non-absorbable 6–0 silk sutures (Ethicon). Mice were housed individually for 60 d. Finally, the mice were sacrificed with cervical dislocation and the samples with surrounding tissue were excised and processed for histological and molecular analysis. All experiments involving animals were conducted according to the protocols of good animal experimentation under the Italian Health Minister approval no 682/2018-PR.

2.13. *In vitro* assay

Whole isolated PBMC were seeded on bioprinted EV-construct to assess the EV ability to induce the adhesion and maturation of EPCs. PBMC were resuspended in M200 complete medium (EV-serum free) and seeded into a 24-well plate (15 × 10^6 cell cm^{-1}) containing EV bioprinted constructs. The cell-seeded scaffolds were cultured for 7 d and the medium was replaced every 48 h. In the *in vitro* assay, the EVs derived from the two extreme cell growth conditions, CM Normoxia and SM Hypoxia, were tested. Finally, the samples were fixed and used for immunofluorescence assay.

2.14. Brightfield acquisition

Explanted constructs were fixed in 4% PFA overnight at 4 °C and washed twice with PBS for 2 h. Then, the samples were decalcified in 200 mM EDTA overnight at RT and placed in μ-Slide (80 426, Ibidi) to acquire brightfield images using Leica time lapse (Leica Microsystem). The image reconstruction was carried out using the mosaic merge tool of LAS X software (Leica Microsystem).

2.15. Immunofluorescence assay

Fixed and decalcified explants were permeabilized with 0.2% TRITON X-100 (Sigma) diluted in PBS for 2 h at 4 °C to gain access to the intracellular antigens. Samples were then incubated in 5% BSA blocking solution for 3 h to saturate the nonspecific sites, and thereafter in anti-von Willebrand Factor (1:100, vWF, 11 713, Abcam) primary antibody diluted in 0.5% BSA solution overnight at 4 °C.

Transversal sections of explants embedded in Killik O.C.T. Compound embedding medium (Bio-Optica, Milan, Italy) were obtained by cryostat

CM1520 (Leica Microsystem, Wetzlar, Germania), placed onto superfrost ultra plus adhesion slides (Thermo Fisher Scientific, Waltham, USA) and incubated with FITC-conjugated lectin BS1-B4 (1:50, L2895, SIGMA) and anti-VE cadherin (1:100, ab33168, Abcam) primary antibodies in 0.5% BSA solution overnight at 4 °C.

Subsequently, the constructs and the sections were incubated with the appropriate secondary conjugated antibody. Nuclei were detected with DAPI (4′,6-Diamidino-2-Phenylindole, Life Technology).

The cell-seeded scaffolds were fixed in 4% PFA for 1 h, permeabilized with 0,1% TRITON X-100 (Sigma) diluted in PBS for 20 min, and incubated in 5% BSA blocking solution for 1 h at RT. Anti-CD31 (ab24590, Abcam), anti-CD45 (560 178, BD Bioscience), and anti-VEGFR2 (AF257, R&D Systems) primary antibodies were used at 1:100 dilution in 0.5% BSA solution for overnight incubation at 4 °C, and detected by the secondary conjugated antibody. TCS SP5 confocal microscope (Leica Microsystem) was employed to acquire the labelled samples using sequential scanning mode.

2.16. Gene expression analysis

Total RNA was extracted from the 3D bioprinted explants. Tissue samples were frozen in liquid nitrogen and homogenized using a pestle and mortar. Then, the samples were incubated in 1 ml of TRIZOL reagent (15 596 026, Invitrogen, Life Technologies) for 5 min at RT to allow complete dissociation of nucleoprotein complexes. A concentration of 0.2 ml of chloroform per ml of TRIZOL was added. Tubes were vigorously shaken for 15 s, incubated at RT for 3 min and centrifuged at 12 000 *g* for 15 min at 4 °C. The aqueous phase was transferred to a fresh tube and RNA was precipitated with 0.5 ml of isopropyl alcohol. After centrifugation, the RNA pellet was washed with 1 ml of 75% ethanol and centrifuged at 7500 *g* for 5 min at 4 °C. At the end of the procedure the RNA pellet was air-dried and dissolved in 30 μl of RNase free water. RNA concentration was determined using a NanoDrop UV–visible spectrophotometer. A 1 μg quantity of total RNA was reverse transcribed to cDNA using a TaqMan Fast Universal PCR Master Mix (11 754-050, Superscript VILO Invitrogen). The evaluation of gene expression was performed by quantitative real-time polymerase chain reaction (qRT-PCR) using a StepOnePlus Real-Time PCR System (Applied Biosystems) (table 1). All reactions were performed in 15 μl reaction volume and in triplicate. The expression data were normalized using the Ct values of the housekeeping mouse gene GAPDH and the control group NO EVs.

2.17. Statistical analysis

Statistical analysis was carried out using Prism 5 (GraphPad Software, La Jolla, CA). Data are presented as mean ± standard deviation (SD). Differences between sample means at each time point were evaluated with Student's *t*-test. A *p*-value <0.05 was considered statistically significant.

3. Results

3.1. HUVEC-derived EV characterization

Our experimental strategy anticipates the use of HUVECs, a commercial line, in order to standardize the starting procedures for all experimental conditions, preventing the interference of uncontrolled variables derived from the use of primary ECs.

In order to identify the best conditions for angiogenic EV production, we grew HUVECs using four different culturing protocols, namely (a) complete M200 medium in normoxia (CM Normoxia); (b) complete M200 medium in hypoxia (CM Hypoxia); (c) serum-free M200 medium in normoxia (SM Normoxia); (d) serum-free M200 medium in hypoxia (SM Hypoxia) (see figure S1 in supplementary information). Following the isolation protocol, EVs were thoroughly analysed using the NanoSight NS300. The particles were analysed individually and simultaneously by direct observation and measurement of diffusion events, generating highly accurate results in terms of EV size, distribution and concentration, highlighting qualitative and quantitative differences (figure 1(A)). The analysis clearly showed a significant increase in the vesicular number produced by a single cell (figure 1(B)) when exposed to both starvation and hypoxia, compared to the other conditions. Furthermore, a significant increase in the production of EVs was observed in the SM Hypoxia culture protocol. EVs were further characterized in terms of size. Interestingly, as shown in figure 1(C), a significant reduction of the particle size mode was observed for the SM Hypoxia condition.

The profile of EVs produced by cells exposed to the combination of starvation and hypoxia was significantly enriched in exosome particles (size 30–100 nm) compared to the other experimental groups. The exosomal fraction has been shown in other studies to be the richest in signalling molecules compared to all other subfamilies of EVs [50] Subsequently, we investigated whether or not these parameters influence tetraspanin expression and overall particle cargo content. Hence, we analysed the expression of specific tetraspanins, namely CD9, CD81, and CD63 [51–54]. For all EV production conditions, we confirmed CD9, CD81, and CD63 expressions on the surface of EVs by FACS analysis (figure 1(D)), and the presence of CD9 and CD81 in the cargo by western blot analysis (figure 1(E)). FACS analysis revealed a reduced CD9 positivity on the membrane of the EVs isolated from HUVECs grown in SM Hypoxia. Conversely, western blot analysis showed an increased CD9 expression in the SM Hypoxia group compared to other conditions. Quantification of CD81, correlated with an enhanced invasion capacity [55],

Table 1. Murine primer sequences for qRT-PCR analysis.

Gene symbol	Sense-forward primer	Antisense-reverse primer
GAPDH	TCCACTCATGGCAAATTCAA	TTTGATGTTAGTGGGGTCTCG
KDR	ACGAGGAGAGAGGGTCATCT	ACACTCTCCTGCTCAGTTGG
E-NOS	GAGATTGGCATGAGGGACCT	GTGTCCAGATCCATGCACAC
PlGF2	GTGTGCCGATAAAGACAGCC	CCTCCTTTCTGCCTTTGTCG
VEGFA	CACGACAGAAGGAGAGCAGA	TCTCAATCGGACGGCAGTAG
VEGFB	CCAAGTCCGAATGCAGATCC	ATTGGCTGTGTTCTTCCAGG
VEGFR1	TCATGTTGGATTGCTGGCAC	TGTTGGACGTTGGCTTGAAG

by FACS and western blot analysis revealed a reduced expression in CM Hypoxia and an increase in SM Hypoxia.

An ELISA test was performed to confirm the angiogenic load differences of the isolated EVs from the four experimental groups. The results clearly demonstrated a defined profile in EV cargo protein expression dependent on cell culture conditions (figure 1(F)). In particular, we noted a significant increase in the SM Hypoxia group in the expression of VEGFR2, which is considered the main transducer of angiogenic signals [56, 57] and PlGF, known to be a key regulator of pathological angiogenesis [58, 59]. At the same time, we observed an increase in the expression of VEGFR1 and VEGF-A in the CM Hypoxia group compared to the others, and a significant reduction of VEGF-A in the SM Hypoxia group. Overall, these results could suggest that such proteic imbalances in the cargo of EVs would prevent or favour ligand–receptor docking once target cells have been reached.

Furthermore, the isolated EVs were analysed by TEM to assess their integrity post-isolation and bioprinting and to identify possible morphological differences among the vesicles derived from HUVECs grown in the four experimental stress conditions. The TEM images in figure 2 confirm the EV identity and dimensions. For all tested conditions, vesicles had similar sizes and shapes revealing intact and regular membranes. Vesicle diameter distributions were similar for all groups: CM Normoxia (14.9–83.6 nm), CM Hypoxia (23.3–89.9 nm), SM Normoxia (26–126.7 nm) and SM Hypoxia (26.7–81.5 nm). Interestingly, the discrepancy in particle size found between the TEM analysis and NanoSight is in agreement with previous studies [60–62]. In fact, the average diameter detected by the NanoSight, for each event, is slightly overestimated compared to that measured by TEM. This phenomenon is due to the operating dynamics of the NanoSight, which are based on the ability to faithfully detect the diffusion of light, but are influenced by other molecules that interact with the vesicle membrane, such as proteins or solvents. On the other hand, TEM suffers from an obvious sampling problem. TEM images are related to a very small part of the sample, and to classify these images as representative, it is necessary to compare these two results to have a faithful distribution of the morphology of the studied samples.

3.2. Bioink printability characterization

The bioinks used in our experiments were formulated by combining two largely used biopolymers—namely ALG (4% w/v) and GelMA (6% w/v)—with a small addition of Irgacure 2959 to ignite radical polymerization of GelMA. EVs derived from different culture conditions were then resuspended in these solutions. The choice of optimal EV concentration was obtained by inserting double the number of vesicles needed for optimal EC repopulation of a $10 \times 4 \times 1$ mm^3 construct [63].

In order to thoroughly characterize our fibre deposition strategy and the formulated bioink, we initially performed a series of printability tests. Specifically, we analysed: (a) the influence of EVs over bioink viscosity, (b) the concentrations of calcium chloride and ALG over bioink printability, (c) the dependence of fibre diameter over printing speed, (d) the possibility of manufacturing scaffolds with different fibre orientations, and (e) the manufacture of a macroscopic, hierarchical vasculature model.

Firstly, we studied the influence of EVs on bioink viscosity using rheological investigations. As shown in figure 3(A), the addition of EVs to ALG-GelMA bioink did not significantly influence its viscosity as the two traces (ALG-GelMA and ALG-GelMA-EVs) almost overlapped (the scale range of the Y-axis is rather small; therefore, the differences between the two traces are of the order of tens of millipascal). Moreover, the behaviour of the final bioink can be approximated to an almost Newtonian fluid with a very weak influence of shear rate on viscosity at low shear rate values. This guarantees that the viscosity of the bioink remains constant during the experiments. After rheological characterization, we investigated the influence of calcium chloride and ALG concentrations on bioink printability. In this case, we performed a series of experiments using different concentrations of the two components while checking for the possibility of finely depositing hydrogel strands. The obtained results are summarized in the heat map shown in figure 3(B): high printability can be obtained along the diagonal that spans from high concentration of calcium chloride and low concentration of ALG to the inverse condition—i.e.

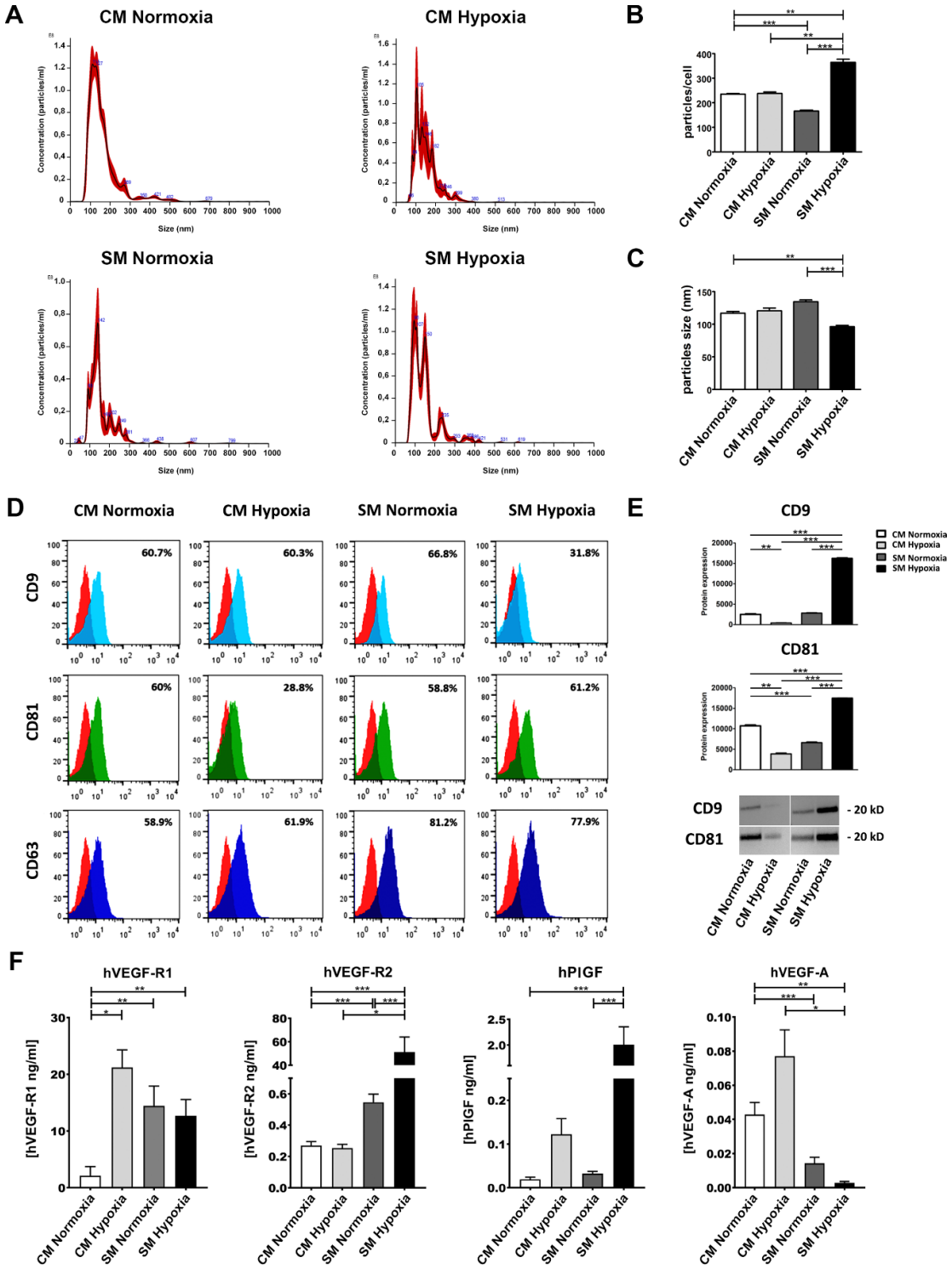

Figure 1. EV characterization. (A) Size distribution profiles of HUVEC-derived EVs in CM Normoxia, CM Hypoxia, SM Normoxia and SM Hypoxia conditions, analysed by NanoSight NS300. (B) Single-cell production of EVs. (C) Histogram chart of the EV modes relative to particle size (nm). (D) Flow cytometry analysis of EV-tetraspanins CD9, CD81, CD63. (E) Representative images of CD9 and CD81 EV-derived proteins determined by western blot analysis and related graphs. (F) Representative histograms of ELISA performed on lysated EV-derived proteins. The analysis has been optimized to detect hVEGF-R1, hVEGF-R2, hPlGF and hVEGF-A angiogenic proteins. Error bars represent ±SD. Student's *t*-test, $^{*}p < 0.05$, $^{**}p < 0.01$, $^{***}p < 0.001$.

high concentration of ALG and low concentration of calcium chloride. These results are in agreement with a similar characterization of ALG-based bioinks [49]. Since the stiffness of the final gels is primarily dependent on ALG concentration, in our experiments we opted for the bottom right condition (high ALG content, low calcium chloride concentration—4% w/v ALG and 0.3 M calcium chloride) to obtain stable and self-standing scaffolds. Once this condition was fixed, we additionally performed a printing speed test to unravel the relation between this parameter and the fibre diameter. As expected, printing

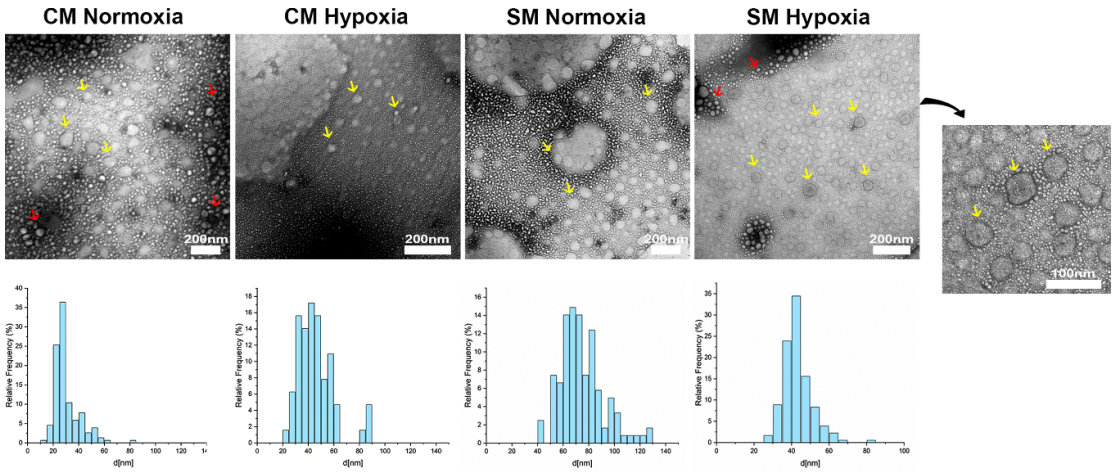

Figure 2. TEM of EVs post-isolation. (Top row) TEM images of the EVs obtained in different conditions. Yellow arrows show the vesicles while red arrows highlight the presence of artifacts. For the sake of quantification, artifacts were excluded from the particle analysis. Higher magnification of EVs, demonstrating their uniformity in size with uninjured membrane, is reported on the right. (Bottom row) Histograms displaying the diameter (nm) distribution of vesicles obtained from different experimental conditions.

speed and fibre diameter are inversely proportional (figure 3(C)), indicating that an increase of speed, at a fixed bioink extrusion rate of 5 μl min^{-1}, entails a reduction of fibre diameter and vice versa. Of note, using a speed of 8 mm s^{-1} enables the deposition of fibres of approximately 100 μm.

After such careful optimization, we ultimately tested our printing set-up for the manufacturing of scaffolds with different fibre orientations and of a macroscale, intricate vasculature model (see figure S4 in supplementary information). In both cases, our printing set-up demonstrated high versatility and robustness through the precise manufacturing of the desired structures.

3.3. Bioprinting of EVs

After bioink printability characterization, we investigated the possibility to obtain homogeneous EV distribution in the bioprinted scaffolds. This feature is crucial as a homogeneous distribution of EVs will guarantee an isotropic environment upon implantation. With this aim, we marked EVs with a commercial dye (deep red) and fabricated scaffolds characterized by parallel fibre orientation (figure 3(D)). In these experiments, we decided to print scaffolds with a unidirectionally aligned orientation of fibres to partially mimic the parallel pattern of arterial and venous vessels, and to provide spatial guidance to the neoforming vessels, due to the high proximity of the bioprinted fibres. As one can see, fluorescence images of the bioprinted constructs containing the EVs labelled with deep red dye revealed a homogeneous distribution of EVs throughout the printed scaffolds (figure 3(F)).

EV distribution in the printed matrices was further investigated by means of SEM and benchmarked against an EV-free scaffold (figure 4). At low magnification, the two matrices appear similar, with an intricate network of porous channels. At high magnification, instead, one can observe that the pore surface is significantly different between the two samples: in fact, the sample containing EVs presents a bumpy surface (with bumps of the size of the EVs) while the EV-free sample is characterized by a smooth one. Finally, we investigated via TEM the influence of the 3D bioprinting procedure on the integrity of the EV membrane (see figure S5 in the supplementary information). This test required the enzymatic digestion of the printed scaffolds to re-isolate EVs. Notably, we found that the EV membrane was not affected by the 3D bioprinting step and the size of the vesicles remained unchanged, thus confirming the high compatibility of our printing strategy with EV encapsulation.

Lastly, we investigated the EV dispersion profile from the bioprinted structures *in vitro* by culturing the constructs from the SM Hypoxia group for 7 d in EV-free medium (figure 4(B)). The graph reported in figure 4(B) shows a minimal EV release with time. After 24 h, the released particles comprise about 8% of the initial amount, reaching a maximum release of 16% after one week. As expected, the released vesicles are very limited, confirming that more than 80% of bioprinted EVs remain in the constructs.

3.4. Subcutaneous transplantation of 3D bioprinted EVs

The bioprinted structures containing EVs isolated from HUVECs cultured in the different modalities were transplanted subcutaneously into immunocompromised NSG mice (see figure S2(A) in supplementary information) to evaluate their angiogenic properties. In this test, each animal used received four different scaffolds out of the five conditions tested (see figure 5). To minimize the bias relative

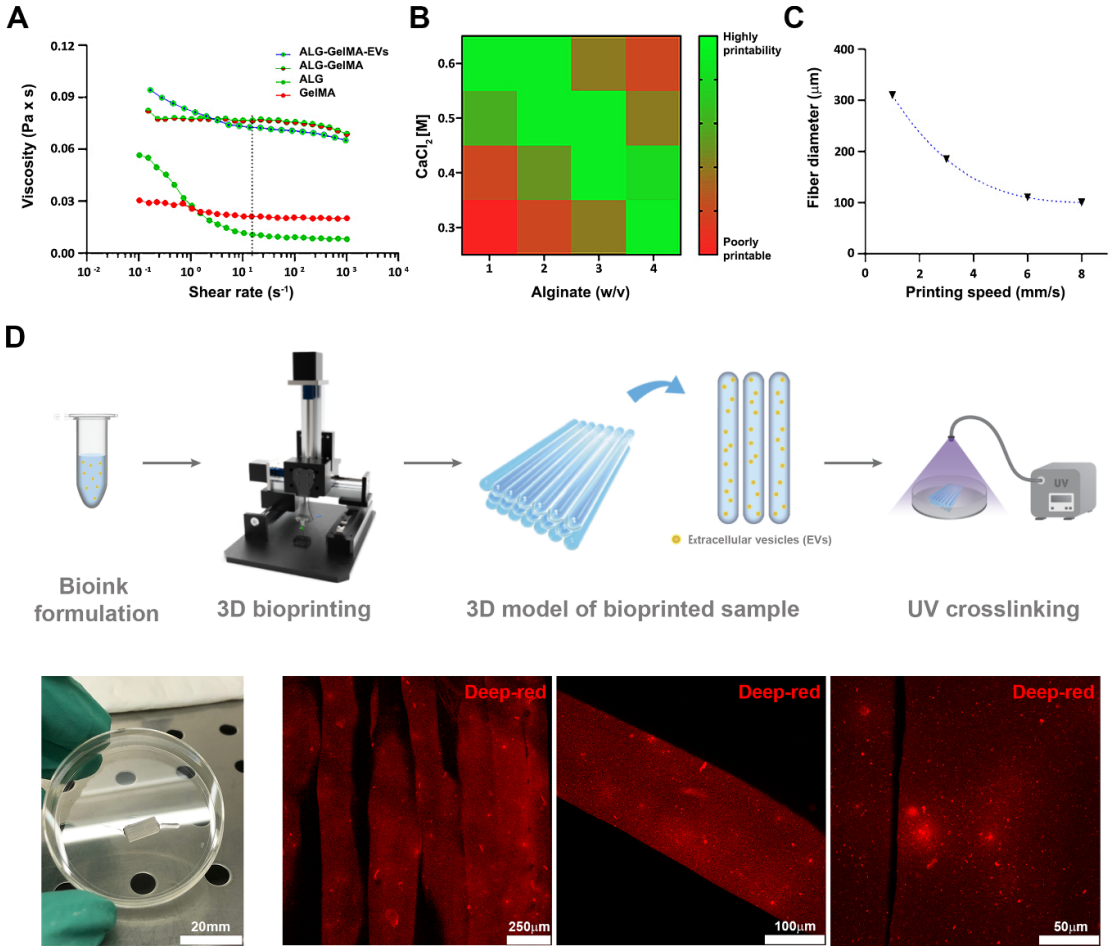

Figure 3. 3D bioprinting. (A) Rheological characterization of the GelMA (red), ALG (green), ALG-GelMA (half green, half red) and ALG-GelMA-EV (green with internal blue dot) solutions; (B) Printability heat map highlighting the best printing conditions in terms of bioink and calcium chloride concentrations. (C) Dependence of deposited fibre diameter on printing speed. (D) Top: schematic representation of the bioprinting process to manufacture EV-loaded scaffolds. Bottom: actual image of a bioprinted sample containing EVs and representative fluorescence images of EVs positive for CellMask Deep Red plasma membrane stain, encapsulated into bioprinted fibres.

to the position, each condition was implanted additionally in dorsal, cranial, and caudal surgical sites. This precaution should prevent engraftment variability due to the different vascularization spots of the dorsal muscle. After 60 d, an extensive network of blood vessels was detected in all animals that received the constructs loaded with the EVs, while the NO EVs control (biomaterial only) did not show any additional vascular network. Furthermore, we observed the presence of a slight calcification due to the limited biodegradation activity of the immune system; however, this did not hamper the blood circulation in the neovasculature (see figure S2(B) in supplementary information). To better appreciate the neovasculatures, explants were decalcified using EDTA (figure 5). Interestingly, we found that the new blood vessels present on the muscular surface of the animals infiltrated the bioprinted constructs, which provided a spatial guide for vessel growth. Among the tested samples, those from the SM Normoxia and SM Hypoxia groups revealed the most abundant and functional neovasculature. Of note, bioprinted structures enabled us to obtain a dense network of secondary branches that interconnect the major vessels transversely. In light of these results, we repeated the experiments using immunocompetent C57/BL6 mice (see figure S3(A) in supplementary information) to validate the angiogenic capacity of EVs in the presence of the host immune system. After 60 d, dorsal implants containing EVs were able to generate extensive neovascularization in the graft areas; however, in this case, the matrix remodelling activity carried out by the host immune system led to rapid hydrogel resorption which reasonably caused a less organized neovasculature (see figure S3(B) in supplementary information).

Finally, we carried out an additional experiment to prove that the 3D architecture of the implants plays a key role itself during the neovascularization process. Specifically, we implanted bulk hydrogels ($10 \times 4 \times 1$ mm^3) with the same chemical composition as the bioprinted ones. In these cases, we observed for all tested conditions a poor, immature and very disorganized vascular network (see figure S6

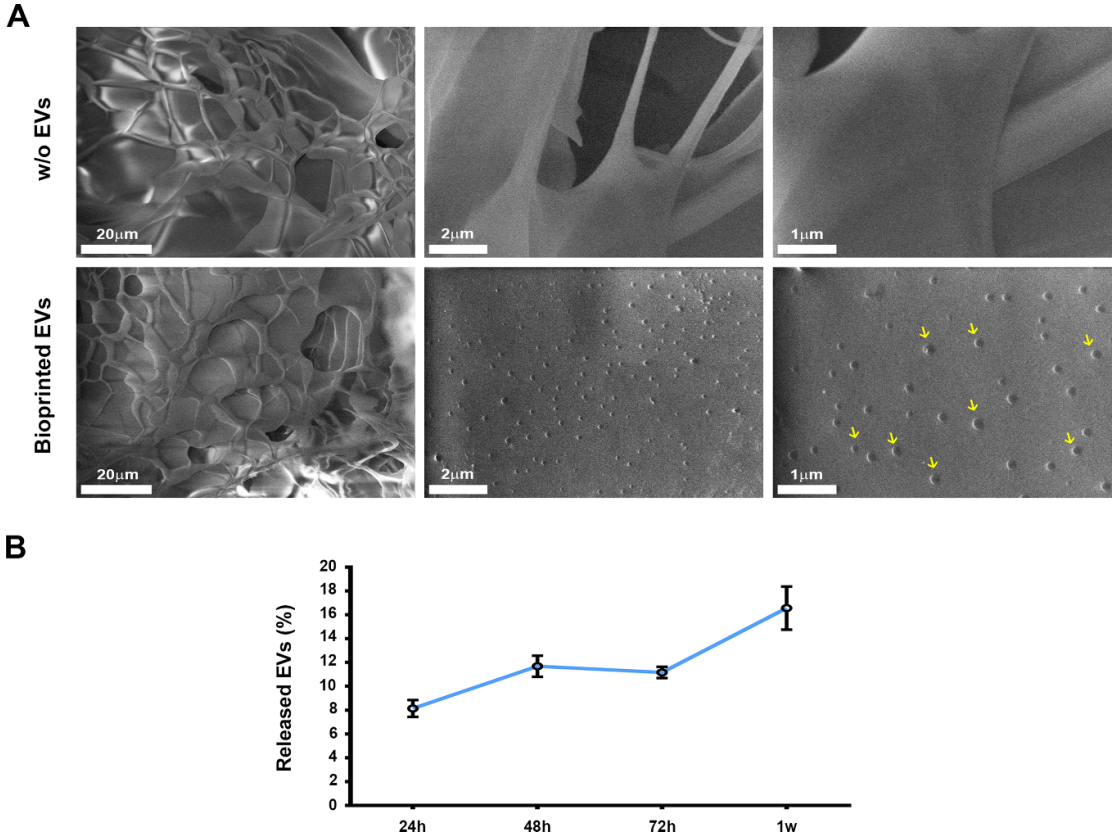

Figure 4. SEM analysis and *in vitro* EV release kinetic assay. (A) SEM images of 3D bioprinted hydrogels (GelMA without EVs and GelMA with EVs). Yellow arrows show a few vesicles. (B) Bioprinted EV dispersion profile in 1 week of culture in EV-free medium.

in supplementary information), thus confirming the added value of the bioprinted architectures.

3.5. Histological analysis

Neovasculatures were further characterized by means of histological analysis. The presence of vessels in the samples was detected using vWF immunostaining. The immunofluorescence assay identified the presence of vessels positive for endothelial antigens running parallel to the hydrogel fibres. High-magnification images allowed us to appreciate the integrity of the vascular structures, especially in the CM Hypoxia, SM Normoxia and SM Hypoxia experimental groups (figure 6). Furthermore, in-depth confocal images, related in particular to the SM Hypoxia group, showed the presence of a well-formed thick vascular network (figure 6), and the presence of several subsegments and branches connecting the larger vessels. Subsequently, the explanted constructs were dissected (figure 7(A)) to evaluate the vessel invasion and branching capacity. In figure 7(B), the positivity of the newly generated vessels for VE-cadherin and Isolectin B4 is reported. Transversal cross-sections of explants enabled us to better appreciate the extended, organized, and well-structured vascular network obtained in the SM Hypoxia condition with respect to the others. Nevertheless, a good degree of vessel infiltration was also observed in the CM Hypoxia and SM Normoxia experimental groups, despite the lower degree of organization. Notably, higher-magnification images revealed the formation of vessel lumens, thus confirming the functional degree of the obtained neovasculature.

Differences in the angiogenesis capacity among the experimental groups were further evaluated quantitatively by counting the number of junctions, segments and branches (figures 8(A) and (B)) using image analysis tools. The results showed a significant increase in the number of junctions induced by bioprinted EVs derived from HUVECs cultivated in starvation and hypoxia (SM Hypoxia) compared to the CM Normoxia and SM Normoxia groups. Furthermore, the starvation/hypoxia experimental group showed a significant increase in branches compared to the other conditions. Moreover, the data highlighted a significantly superior presence of segments in both starved groups compared to the complete medium normoxia condition (figure 8(A)). Altogether, these results demonstrated that the cargo of the EVs produced by cells in hypoxia conditions induced a higher angiogenic stimulus. Finally, in figure 8(C) one can appreciate the presence of cells inside a vessel during the vessel-formation phase.

3.6. Gene expression analysis

qRT-PCR analysis was performed to study the differences in angiogenesis-related gene expression. All the results were normalized on the expression of GAPDH

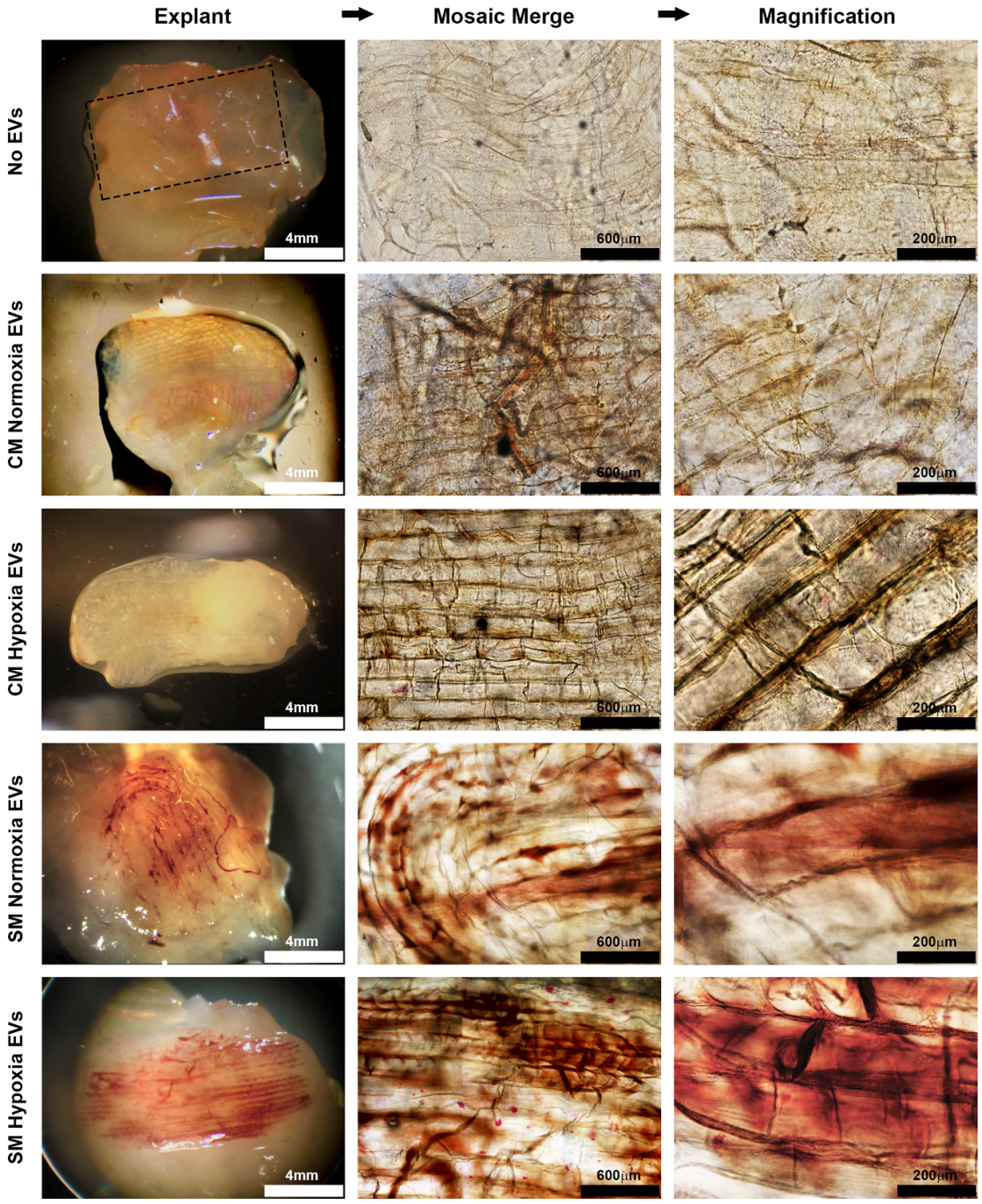

Figure 5. Explants after the decalcification process. Representative images of explanted neovascular networks for each experimental condition tested after EDTA decalcification treatment.

and the control group NO EVs. We detected the expression of nitric oxide endothelial synthase (E-NOS), VEGFR1, VEGFB, VEGFA, PlGF and VEGFR2 (KDR) in all groups. Results showed that KDR expression is significantly silenced in starvation hypoxia samples and E-NOS gene expression is reduced in SM Normoxia compared to SM Hypoxia and CM Normoxia. In contrast, an increase in KDR level was observed in the CM Normoxia group compared to the others, while VEGFA expression was increased only in the CM Hypoxia samples (figure 8(D)). Our data are also supported by other studies claiming that the EVs generated by cell sources cultured in hypoxic conditions perform better in carrying out a defined task compared to cells grown in normoxia [38, 64], but this is the first time that the angiogenic capacity is tested in combination with a 3D bioprinting approach to promote an *in vivo* neovasculature.

3.7. *In vitro* validation

To better elucidate the mechanism by which EVs are able to support the formation of new blood vessels *in vivo*, we conducted *in vitro* experiments using a reverse strategy. We speculated that HUVEC-derived EVs could recall EPCs and induce their terminal differentiation *in loco*. To prove the correctness of

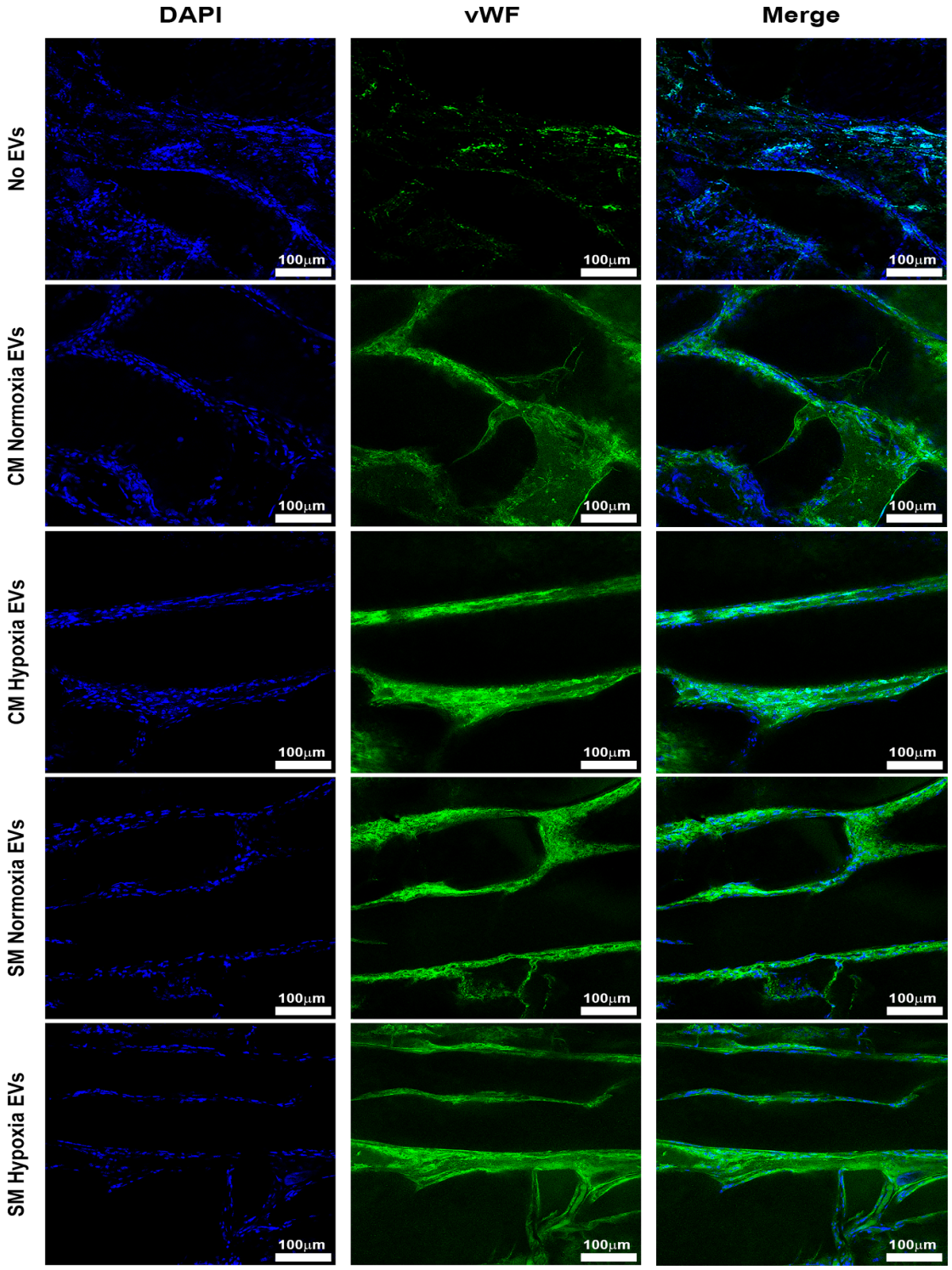

Figure 6. Immunofluorescence assay. Confocal images of explanted bioengineered vessels obtained for NO EVs, CM Normoxia, CM Hypoxia, SM Normoxia, SM Hypoxia groups. The vascular structures were stained for vWF marker, labelled in green. Nuclei were counterstained with DAPI (blue).

this hypothesis, peripheral blood mononuclear cells (PBMCs) containing the EPC fraction were isolated from blood samples from healthy donors by a defined protocol [65]. EVs derived from CM Normoxia and SM Hypoxia conditions were bioprinted directly in the culture dishes, maintaining the same geometries used for *in vivo* experiments. Subsequently, the PBMCs were seeded in the dishes containing the constructs and cultured for 7 d (figure 9(A)). The maturation of EPCs and the formation of spindle-shaped multicellular structures were observed exclusively along the bioprinted EV-containing fibres derived from HUVECs grown in SM Hypoxia and not from those derived from the CM Normoxia control group (figure 9(B)). The endothelial origin of the tubular structures was

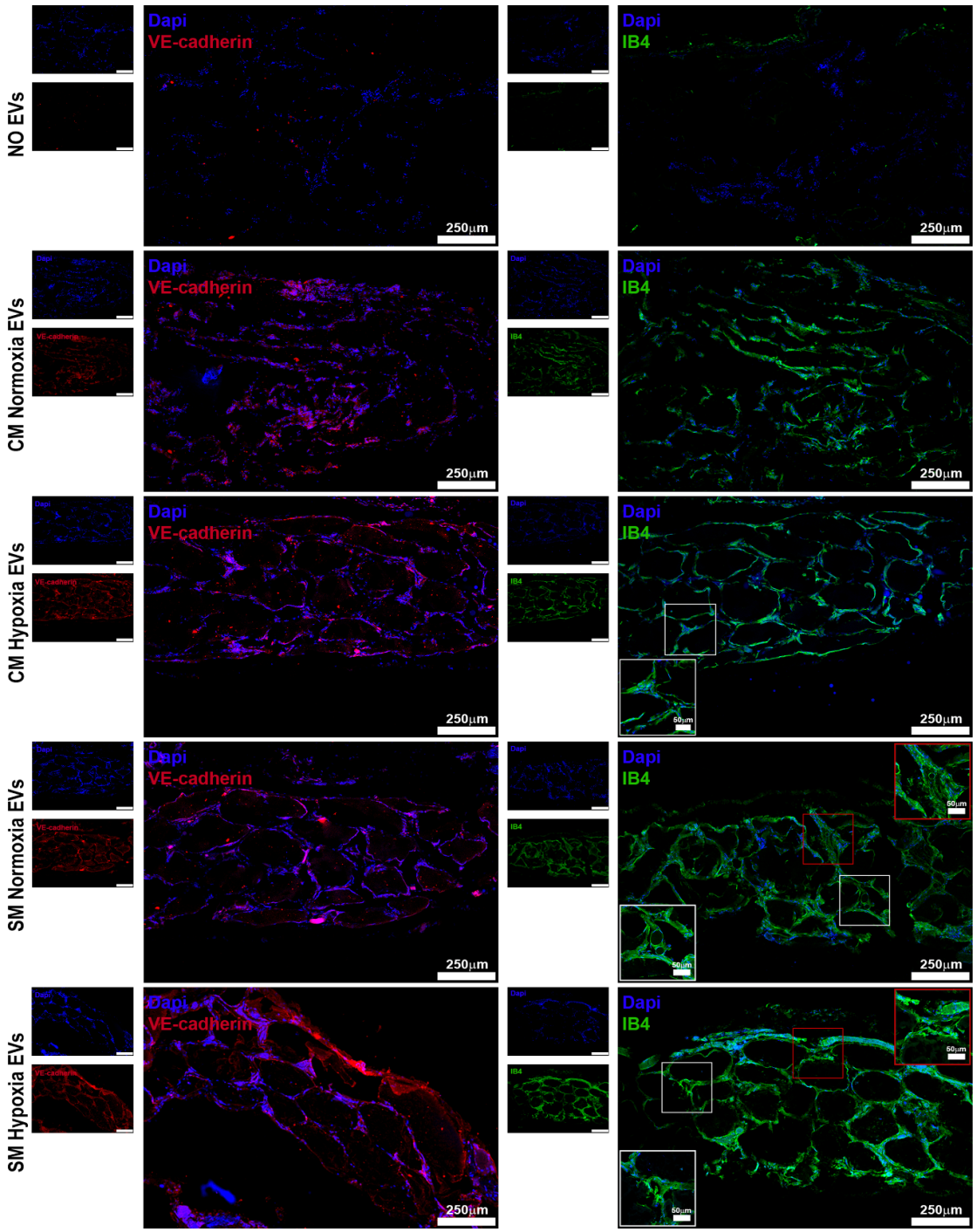

Figure 7. Transversal cross-sections of the explants. Confocal images of transversal sections of explanted bioengineered structures for the NO EVs, CM Normoxia, CM Hypoxia, SM Normoxia, and SM Hypoxia groups. The VE-cadherin positive vessels are labelled in red (left panels), whereas the vessels positive for Isolectin B4 are shown in green (right panels). Nuclei were counterstained with DAPI (blue). Insets show higher-magnification images in which vessel lumens can be appreciated.

confirmed by immunofluorescence assays, resulting positive for CD31, VEGFR2 and CD45 (figure 9(C)). The data obtained *in vitro* validate the results *in vivo*, confirming the ability of EVs derived from SM Hypoxia to stimulate greater organization and maturation of EPCs compared to all other conditions and that the guidance imposed by the printing process allows a fine resolution of neo-angiogenic texture.

4. Discussion

The generation of transplantable engineered tissues for clinical purposes is the most ambitious goal of 3D bioprinting technology. Many efforts have been made in recent years to recapitulate the complexity of biological tissues in terms of macromolecular composition, ultrastructural organization and cell–environment interactions. However,

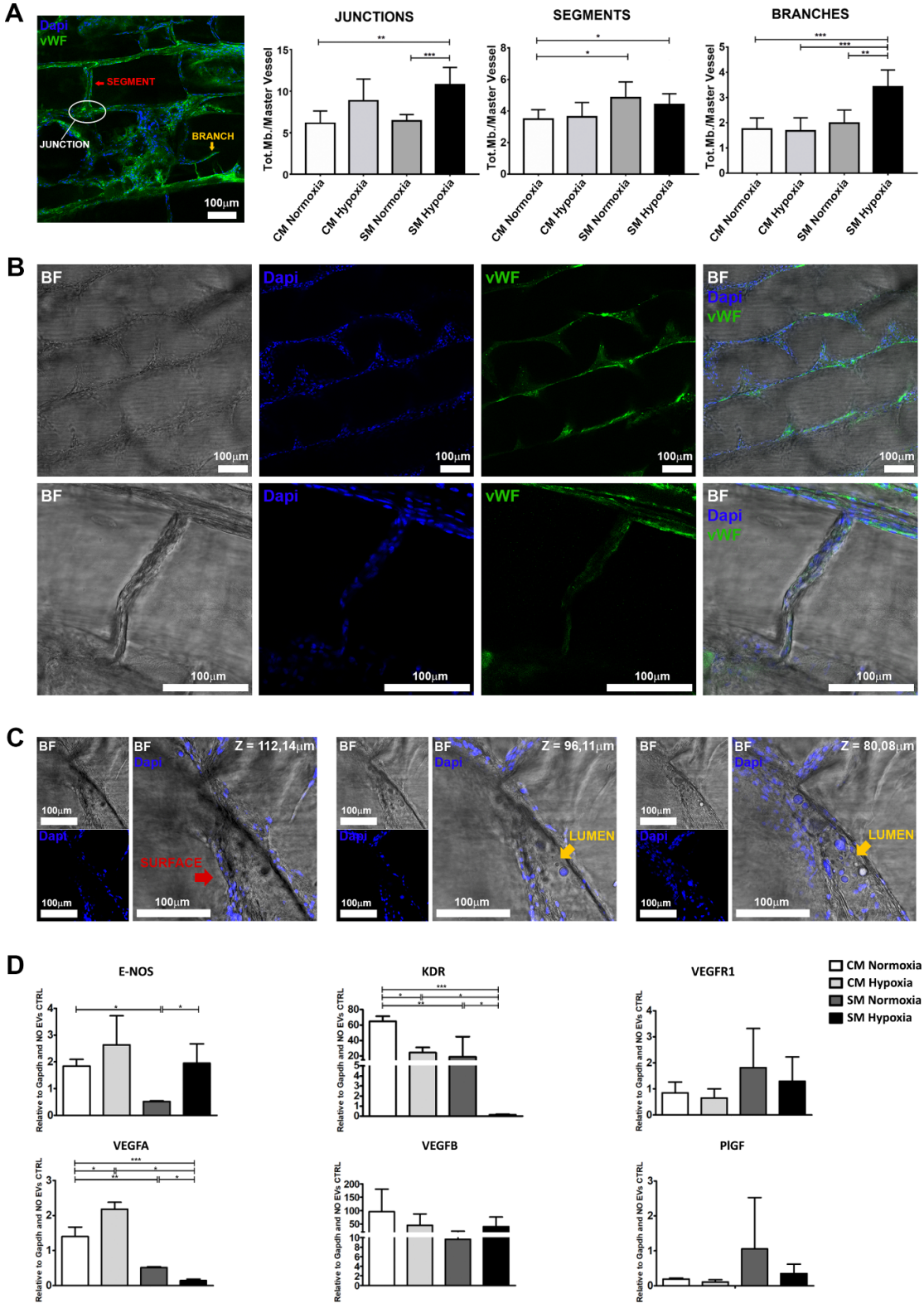

Figure 8. Angiogenesis assessment. (A) Immunofluorescence image of vWF positive vessels. The number of junctions, segments and branches formed by ECs *in vivo* into the constructs is shown in the histograms. (B) Higher magnification of representative branches and segments, positive for vWF (green) obtained for the SM Hypoxia condition. (C) Z-stack acquisition images of vessel formation in the SM Hypoxia group. (D) Gene expression analysis of key markers related to the *in vivo* angiogenic process (E-NOS, KDR, VEGFA, VEGFR1, VEGFB, PlGF). Error bars represent ±SD. Student's *t*-test, $*p < 0.05$, $**p < 0.01$, $***p < 0.001$.

immunorejection and functional engraftment are two variables that make it difficult. The rationale of our study concerns the use of EVs as a bioadditive to promote the neovascularization of bioprinted tissues, maximizing their engraftment capacity and eluding the host immune system. The heterogeneous family of EVs is generated by different subcellular compartments by all human cells [66]. The EVs are able

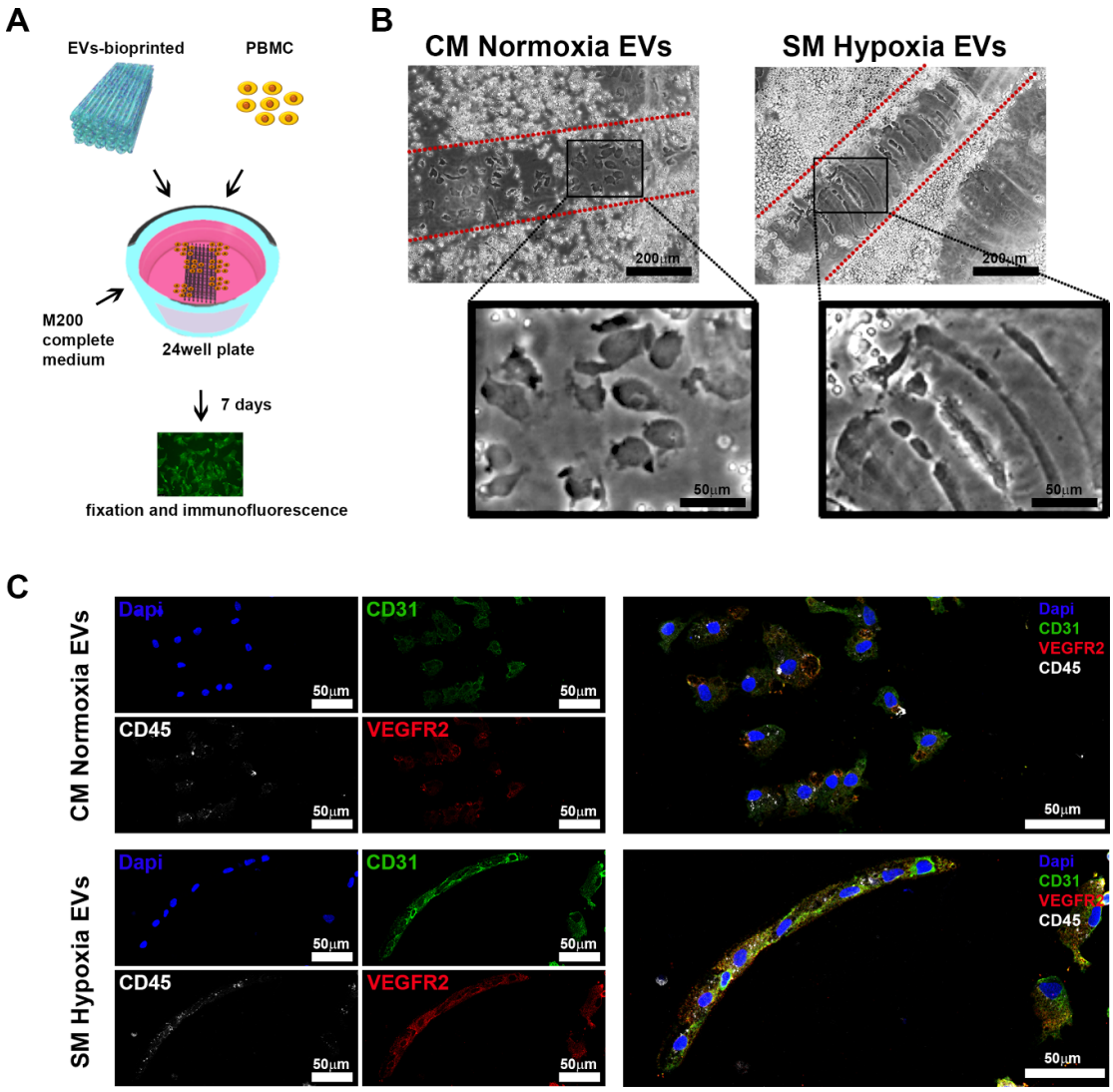

Figure 9. *In vitro* validation. (A) Graphical scheme of *in vitro* assay strategy. PBMC were seeded on bioprinted EVs and cultured for 7 d. (B) Brightfield images of EPCs on the surface of the fibres containing EVs generated from HUVECs in CM Normoxia and SM Hypoxia conditions. (C) Staining for CD31 (green), VEGFR2 (red), CD45 (white) identifying EPCs on the surfaces of bioprinted constructs.

to influence the function and phenotype [11, 17] of target cells transferring bioactive molecules [12–16] derived from the origin population. The role of EC-derived EVs has been elucidated in critical biological processes, i.e. vasculogenesis, inflammation, tissue homeostasis and cardiovascular pathologies related to signalling [67]. In the present study, HUVEC-derived EVs were characterized for angiogenic factors and employed in combination with 3D bioprinting to form a simple yet robust method to promote implant neovascularization *in vivo*, a feature highly needed in regenerative medicine applications. The growing interest in EVs has led to a greater knowledge of their function and awareness of their applicative potential in different scientific research and clinical fields [8, 29, 67]. Moreover, these particles are well tolerated *in vivo* and generally do not elicit any side immunoreaction, thus being an ideal candidate for future clinical translation.

The results obtained in this study can be interpreted as an essential step in this direction, indicating that clinical and regenerative EV applications may be feasible shortly. It is already known in the literature that the production of EVs is enhanced in hypoxic conditions compared to normoxic ones [38], but this is the first time that the angiogenic capacity is explored using a 3D bioprinting approach. HUVECs, as a source of EVs, were exposed to a combination of stressful stimuli, i.e. starvation and hypoxia, inducing the selection of an exosomal profile of the EVs with significant angiogenic potential. The stress stimuli exposition effectiveness was accompanied by an increase of CD9 and CD81 Tetraspanins in EV -cargo observed through western blot analysis. Tetraspanins are a protein superfamily that organizes membrane microdomains called tetraspanin-enriched microdomains by forming clusters and interacting with a wide variety of

transmembrane and cytosolic signalling proteins. This family of proteins is involved in cell adhesion, invasion motility, membrane fusion and especially protein trafficking. CD9 was indicated by Kamisasanuki *et al* as a mediator of stimulus-independent angiogenic effects in ECs, suggesting CD9 as a potential target for antiangiogenic therapies [68]. Therefore, the exposure to CD9 and the internalization modulation we observed could be a consequence of the involvement of CD9 in protein trafficking and selective loading of EVs. Instead, Zhang *et al* reported that CD81 has an oncogenic role in prostatic cancer, correlating the CD81 increase with a greater metastatic ability [55]. Consequently, CD81 may be involved in facilitating the permeability of cells in blood vessels; however, further studies are needed to better understand the function of CD81. The same stressful culture conditions generated a significant enrichment in two major pro-angiogenic protein effectors, namely PlGF and VEGFR2. VEGFR2 is considered the main transducer of angiogenic signals, mediating mitogenic, chemotactic and pro-survival effects on ECs [56, 57], while PlGF is well known to be a key regulator of pathological angiogenesis [58, 59], able to activate VEGFR2 through the crosstalk between its specific receptors VEGFR1 and VEGFR2, amplifying the VEGF response and inducing the expression of VEGF in the recipient cells, further amplifying this synergism [58, 69]. Then, we explored the potential of HUVEC-derived EVs supported by bioprinted GelMA hydrogels to induce rapid vasculogenesis in a host organism. Accordingly, EVs were loaded in 3D hydrogel structures that provide anchorage and protection from physiological biodegradation mechanisms, and spatially guide the vasculogenesis thanks to their organized architectures. We printed the EVs using a custom-made microextrusion bioprinter (CeciliaOpenOrgan 2.0) in a defined parallel pattern, simulating the parallel arterial and venous organization. After 60 d, we observed a massive presence of functional blood-filled vessels, particularly in the SM Hypoxia group. Moreover, the histological analysis of the explanted plugs clearly defined the presence of vascular network both outside and inside the bioprinted structures. This result demonstrates the ability of the EVs to attract the host precursor cells, generating an anchored and organized circulatory system. Interestingly, the neovasculature self-assembled around the bioprinted structures, thus generating a well-organized vessel network especially in the SM Hypoxia condition, resulting in a greater vascular network maturation and number of branches. This aspect is consistent with the literature and is attributable to the greater transfer of cytokines and functional proteins by EVs released in hypoxia that involves a superior capacity of invasion, migration, and proliferation in recipient cells [38, 40, 42]. This feature is of high importance and should be further investigated as tailored 3D architectures could be developed in the future to precisely guide the neovascularization process within bioprinted engineered constructs.

Our initial hypothesis has been validated by *in vitro* experiments using healthy donors' blood-derived EPCs, which were seeded on EV-loaded bioprinted constructs. The EPCs seeded on SM Hypoxia-derived bioprinted EVs revealed a better organization and an increased differentiation capacity after 7 d of culture, developing multicellular fusiform structures similar to microvessels on the surfaces of the fibres.

A powerful aspect of the presented approach is to drive the EV-induced effects in a specific site through the anchoring provided by the bioprinted hydrogel. This is in contrast with the conventional uses of EVs *in vivo* based on systemic administration or simple *in situ* inoculation. This important feature, to date, has limited the development of EV-based therapeutic approaches. Further studies will be needed to translate this strategy into actual clinical scenarios, ensuring patient safety and standardizing cell culture procedures.

5. Conclusions

To our knowledge, this is the first study that combines a bioprinting approach with the formulation of a bioink based on bioactive EVs. Our strategy allowed us to precisely manipulate and control the spatial localization of EVs in a 3D matrix, bypassing the current limitations of random biodistribution *in vivo*, and obtaining the greatest expression of their intrinsic angiogenic potential. Furthermore, the presented innovative bioink could be an extremely useful tool for all biofabricated tissues by supporting their rapid engraftment in scar and fibrotic areas in case of transplantation, or even just to obtain rapid revascularization of ischaemic tissues. However, additional efforts should be directed towards the development of standardization protocols for the clinical-grade production of EVs. We believe that the formulation of bioinks supplemented by EVs is an area worth further exploration which, eventually, could be useful to boost the development of spare tissues for clinical purposes by addressing the long-standing challenge in tissue engineering of microvasculature integration.

Acknowledgments

This research was funded by Regione Lazio, LAZIO INNOVA (85-2017-15095) and by the Italian Regenerative Medicine Infrastructure (IRMI), Cluster ALISEI (CTN01_00177_888744). This study was also supported by the National Science Centre Poland (NCN) within SONATA 14 Project No. 2018/31/D/ST8/03647 to MC. We are grateful to

Chiara Cordiglieri and INGM Imaging Facility for their assistance during image acquisition.

Ethical statement

Blood samples were obtained from patients that had given their informed consent for use of the remaining samples after diagnosis for noninterventional, observational research studies. Patients understood that data resulting from the analysis could be published. Approval from an institutional review board (ethics committee) was not needed, since neither direct human participation nor involvement of human studies were involved in this work.

ORCID iDs

Marco Costantini https://orcid.org/0000-0003-2756-5872
Roberto Rizzi https://orcid.org/0000-0001-6084-7199

References

[1] Ionov L 2018 4D biofabrication: materials, methods, and applications *Adv. Healthcare Mater.* **7** e1800412
[2] Moroni L *et al* 2018 Biofabrication: a guide to technology and terminology *Trends Biotechnol.* **36** 384–402
[3] Mota C, Puppi D, Chiellini F and Chiellini E 2015 Additive manufacturing techniques for the production of tissue engineering constructs *J. Tissue Eng. Regen. Med.* **9** 174–90
[4] Datta P, Ayan B and Ozbolat I T 2017 Bioprinting for vascular and vascularized tissue biofabrication *Acta Biomater.* **51** 1–20
[5] Moroni L *et al* 2018 Biofabrication strategies for 3D *in vitro* models and regenerative medicine *Nat. Rev. Mater.* **3** 21–37
[6] Mause S F and Weber C 2010 Microparticles: protagonists of a novel communication network for intercellular information exchange *Circ. Res.* **107** 1047–57
[7] Lamichhane T N, Sokic S, Schardt J S, Raiker R S, Lin J W and Jay S M 2015 Emerging roles for extracellular vesicles in tissue engineering and regenerative medicine *Tissue Eng. Part B* **21** 45–54
[8] De Jong O G, Van Balkom B W M, Schiffelers R M, Bouten C V C and Verhaar M C 2014 Extracellular vesicles: potential roles in regenerative medicine *Front. Immunol.* **5** 608
[9] Lee R T and Walsh K 2016 The future of cardiovascular regenerative medicine *Circulation* **133** 2618–25
[10] Sampogna G, Guraya S Y and Forgione A 2015 Regenerative medicine: historical roots and potential strategies in modern medicine *J. Microsc. Ultrastruct.* **3** 101–7
[11] Sahoo S *et al* 2011 Exosomes from human CD34(+) stem cells mediate their proangiogenic paracrine activity *Circ. Res.* **109** 724–8
[12] Skog J, Würdinger T, van Rijn S, Meijer D H, Gainche L, Curry W T, Carter B S, Krichevsky A M and Breakefield X O 2008 Glioblastoma microvesicles transport RNA and proteins that promote tumour growth and provide diagnostic biomarkers *Nat. Cell Biol.* **10** 1470–6
[13] Tokarz A *et al* 2015 Extracellular vesicles participate in the transport of cytokines and angiogenic factors in diabetic patients with ocular complications *Folia Med. Cracov* **55** 35–48
[14] Valadi H, Ekström K, Bossios A, Sjöstrand M, Lee J J and Lötvall J O 2007 Exosome-mediated transfer of mRNAs and microRNAs is a novel mechanism of genetic exchange between cells *Nat. Cell Biol.* **9** 654–9
[15] Zernecke A *et al* 2009 Delivery of microRNA-126 by apoptotic bodies induces CXCL12-dependent vascular protection *Sci. Signal* **2** ra81
[16] Kogure T, Yan I K, Lin W-L and Patel T 2013 Extracellular vesicle-mediated transfer of a novel long noncoding RNA TUC339: a mechanism of intercellular signaling in human hepatocellular cancer *Gen. Cancer* **4** 261–72
[17] Baci D *et al* 2020 Extracellular vesicles from skeletal muscle cells efficiently promote myogenesis in induced pluripotent stem cells *Cells* **9** 1527
[18] Margolis L and Sadovsky Y 2019 The biology of extracellular vesicles: the known unknowns *PLoS Biol.* **17** e3000363
[19] Latifkar A *et al* 2019 New insights into extracellular vesicle biogenesis and function *J Cell Sci* **132** : jcs222406
[20] Harding C, Heuser J and Stahl P 1983 Receptor-mediated endocytosis of transferrin and recycling of the transferrin receptor in rat reticulocytes *J. Cell Biol.* **97** 329–39
[21] Simpson R J, Lim J W, Moritz R L and Mathivanan S 2009 Exosomes: proteomic insights and diagnostic potential *Expert Rev. Proteomics* **6** 267–83
[22] Rautou P E *et al* 2011 Microparticles from human atherosclerotic plaques promote endothelial ICAM-1-dependent monocyte adhesion and transendothelial migration *Circ. Res.* **108** 335–43
[23] Lo S C, Hung C-Y, Lin D-T, Peng H-C and Huang T-F 2006 Involvement of platelet glycoprotein Ib in platelet microparticle mediated neutrophil activation *J. Biomed. Sci.* **13** 787–96
[24] Dasgupta S K, Abdel-Monem H, Niravath P, Le A, Bellera R V, Langlois K, Nagata S, Rumbaut R E and Thiagarajan P 2009 Lactadherin and clearance of platelet-derived microvesicles *Blood* **113** 1332–9
[25] Dasgupta S K, Le A, Chavakis T, Rumbaut R E and Thiagarajan P 2012 Developmental endothelial locus-1 (del-1) mediates clearance of platelet microparticles by the endothelium *Circulation* **125** 1664–72
[26] Mulcahy L A, Pink R C and Carter D R 2014 Routes and mechanisms of extracellular vesicle uptake *J. Extracell. Vesicles* **3** 24641
[27] Xu D and Tahara H 2013 The role of exosomes and microRNAs in senescence and aging *Adv. Drug Deliv. Rev.* **65** 368–75
[28] Todorova D, Simoncini S, Lacroix R, Sabatier F and Dignat-George F 2017 Extracellular vesicles in angiogenesis *Circ. Res.* **120** 1658–73
[29] Kikuchi S, Yoshioka Y, Prieto-Vila M and Ochiya T 2019 Involvement of extracellular vesicles in vascular-related functions in cancer progression and metastasis *Int. J. Mol. Sci.* **20** 2584
[30] Le Bihan M C *et al* 2012 In-depth analysis of the secretome identifies three major independent secretory pathways in differentiating human myoblasts *J. Proteomics* **77** 344–56
[31] Rome S, Forterre A, Mizgier M L and Bouzakri K 2019 Skeletal muscle-released extracellular vesicles: state of the art *Front. Physiol.* **10** 929
[32] Ko S Y *et al* 2019 Cancer-derived small extracellular vesicles promote angiogenesis by heparin-bound, bevacizumab-insensitive VEGF, independent of vesicle uptake *Commun Biol* **2** 386
[33] Ludwig N *et al* 2018 Exosomes from HNSCC promote angiogenesis through reprogramming of endothelial cells *Mol Cancer Res.* **16** 1798–808
[34] Taraboletti G, D'Ascenzo S, Borsotti P, Giavazzi R, Pavan A and Dolo V 2002 Shedding of the matrix metalloproteinases MMP-2, MMP-9, and MT1-MMP as membrane vesicle-associated components by endothelial cells *Am. J. Pathol.* **160** 673–80
[35] Sheldon H *et al* 2010 New mechanism for notch signaling to endothelium at a distance by delta-like 4 incorporation into exosomes *Blood* **116** 2385–94
[36] Arderiu G, Peña E and Badimon L 2015 Angiogenic microvascular endothelial cells release microparticles rich in tissue factor that promotes postischemic collateral vessel

formation *Arteriosclerosis Thromb. Vasc. Biol.* **35** 348–57
[37] Stamatovic S M, Keep R F, Mostarica-Stojkovic M and Andjelkovic A V 2006 CCL2 regulates angiogenesis via activation of Ets-1 transcription factor *J. Immunol.* **177** 2651–61
[38] Bister N, Pistono C, Huremagic B, Jolkkonen J, Giugno R and Malm T 2020 Hypoxia and extracellular vesicles: a review on methods, vesicular cargo and functions *J. Extracell. Vesicles* **10** e12002
[39] Mleczko J, Ortega F J, Falcon-Perez J M, Wabitsch M, Fernandez-Real J M and Mora S 2018 Extracellular vesicles from hypoxic adipocytes and obese subjects reduce insulin-stimulated glucose uptake *Mol. Nutrition Food Res.* **62** 1700917
[40] Salomon C, Ryan J, Sobrevia L, Kobayashi M, Ashman K, Mitchell M and Rice G E 2013 Exosomal signaling during hypoxia mediates microvascular endothelial cell migration and vasculogenesis *PLoS One* **8** e68451
[41] Ramteke A, Ting H, Agarwal C, Mateen S, Somasagara R, Hussain A, Graner M, Frederick B, Agarwal R and Deep G 2015 Exosomes secreted under hypoxia enhance invasiveness and stemness of prostate cancer cells by targeting adherens junction molecules *Mol. Carcinog* **54** 554–65
[42] Burnley-Hall N, Willis G, Davis J, Rees D A and James P E 2017 Nitrite-derived nitric oxide reduces hypoxia-inducible factor 1α-mediated extracellular vesicle production by endothelial cells *Nitric Oxide* **63** 1–12
[43] Wiklander O P B *et al* 2015 Extracellular vesicle *in vivo* biodistribution is determined by cell source, route of administration and targeting *J. Extracell. Vesicles* **4** 26316
[44] Manca M L *et al* 2016 Glycerosomes: use of hydrogenated soy phosphatidylcholine mixture and its effect on vesicle features and diclofenac skin penetration *Int. J. Pharm.* **511** 198–204
[45] Smyth T, Kullberg M, Malik N, Smith-Jones P, Graner M W and Anchordoquy T J 2015 Biodistribution and delivery efficiency of unmodified tumor-derived exosomes *J. Control. Release* **199** 145–55
[46] Gurunathan S, Kang M-H, Jeyaraj M, Qasim M and Kim J-H 2019 Review of the isolation, characterization, biological function, and multifarious therapeutic approaches of exosomes *Cells* **8** 307
[47] Thery C *et al* 2006 Isolation and characterization of exosomes from cell culture supernatants and biological fluids *Curr. Protoc. Cell Biol.* **30** 3.22.1–29
[48] Borzi C, Calzolari L, Ferretti A M, Caleca L, Pastorino U, Sozzi G and Fortunato O 2019 c-Myc shuttled by tumour-derived extracellular vesicles promotes lung bronchial cell proliferation through miR-19b and miR-92a *Cell Death Dis.* **10** 759
[49] Colosi C, Shin S R, Manoharan V, Massa S, Costantini M, Barbetta A, Dokmeci M R, Dentini M and Khademhosseini A 2016 Microfluidic bioprinting of heterogeneous 3D tissue constructs using low-viscosity bioink *Adv. Mater.* **28** 677–84
[50] Zhang Y, Liu Y, Liu H and Tang W H 2019 Exosomes: biogenesis, biologic function and clinical potential *Cell Biosci.* **9** 19
[51] Hemler M E 2005 Tetraspanin functions and associated microdomains *Nat. Rev. Mol. Cell Biol.* **6** 801–11
[52] Yáñez-Mó M, Barreiro O, Gordon-Alonso M, Sala-Valdés M and Sánchez-Madrid F 2009 Tetraspanin-enriched microdomains: a functional unit in cell plasma membranes *Trends Cell Biol.* **19** 434–46
[53] Hemler M E 2008 Targeting of tetraspanin proteins—potential benefits and strategies *Nat. Rev. Drug Discovery* **7** 747–58
[54] Hemler M E 2001 Specific tetraspanin functions *J. Cell Biol.* **155** 1103–7
[55] Zhang Y *et al* 2020 Increased expression of CD81 is associated with poor prognosis of prostate cancer and increases the progression of prostate cancer cells *in vitro Exp. Ther. Med.* **19** 755–61
[56] Claesson-Welsh L 2003 Signal transduction by vascular endothelial growth factor receptors *Biochem. Soc. Trans.* **31** 20–24
[57] Ferrara N, Gerber H P and LeCouter J 2003 The biology of VEGF and its receptors *Nat. Med.* **9** 669–76
[58] Carmeliet P *et al* 2001 Synergism between vascular endothelial growth factor and placental growth factor contributes to angiogenesis and plasma extravasation in pathological conditions *Nat. Med.* **7** 575–83
[59] Autiero M *et al* 2003 Role of PlGF in the intra- and intermolecular cross talk between the VEGF receptors Flt1 and Flk1 *Nat. Med.* **9** 936–43
[60] Noble J M, Roberts L M, Vidavsky N, Chiou A E, Fischbach C, Paszek M J, Estroff L A and Kourkoutis L F 2020 Direct comparison of optical and electron microscopy methods for structural characterization of extracellular vesicles *J. Struct. Biol.* **210** 107474
[61] Bachurski D *et al* 2019 Extracellular vesicle measurements with nanoparticle tracking analysis—an accuracy and repeatability comparison between NanoSight NS300 and zetaview *J Extracell Vesicles* **8** 1596016
[62] van der Pol E, Coumans F A W, Grootemaat A E, Gardiner C, Sargent I L, Harrison P, Sturk A, van Leeuwen T G and Nieuwland R 2014 Particle size distribution of exosomes and microvesicles determined by transmission electron microscopy, flow cytometry, nanoparticle tracking analysis, and resistive pulse sensing *J. Thromb. Haemost* **12** 1182–92
[63] Maiullari F and Costantini M 2018 A multi-cellular 3D bioprinting approach for vascularized heart tissue engineering based on HUVECs and iPSC-derived cardiomyocytes *Sci Rep.* **8** 13532
[64] Shao C, Yang F, Miao S, Liu W, Wang C, Shu Y and Shen H 2018 Role of hypoxia-induced exosomes in tumor biology *Mol. Cancer* **17** 120
[65] Rahmoune H and Guest P C 2018 Studies of isolated peripheral blood cells as a model of immune dysfunction *Methods Mol. Biol.* **1735** 221–9
[66] Oggero S, Austin-Williams S and Norling L V 2019 The contrasting role of extracellular vesicles in vascular inflammation and tissue repair *Front. Pharmacol.* **10** 1479
[67] Hafiane A and Daskalopoulou S S 2018 Extracellular vesicles characteristics and emerging roles in atherosclerotic cardiovascular disease *Metabolism* **85** 213–22
[68] Kamisasanuki T *et al* 2011 Targeting CD9 produces stimulus-independent antiangiogenic effects predominantly in activated endothelial cells during angiogenesis: a novel antiangiogenic therapy *Biochem. Biophys. Res. Commun.* **413** 128–35
[69] Tjwa M, Luttun A, Autiero M and Carmeliet P 2003 VEGF and PlGF: two pleiotropic growth factors with distinct roles in development and homeostasis *Cell Tissue Res.* **314** 5–14